3 Principles of the Determination of Elastic Properties

3.1 Creep Recovery Experiment and Retardation Spectrum

Elastic properties manifest themselves in many effects. In principle, each of them could be used to get insight into the elastic behavior of a material. A rather obvious feature of elastic properties is the recovery of some of the deformation previously exerted on a sample, when the deforming stress is released. For quantitative measurements, the deformation and the recovery as well have to be performed under certain conditions. A convenient method is creep and the subsequent creep recovery. The principle of such a test is sketched in Figure 3.1. At the time $t = 0$ a sample is loaded by a constant stress and the deformation registered as a function of time. After the creep time t_0 the stress is set to zero. For a viscoelastic sample, some of the total deformation recovers before attaining a time-independent level. This plateau is due to the irreversible viscous deformation of the sample and the recoverable portion has its origin in the elastic behavior of the material.

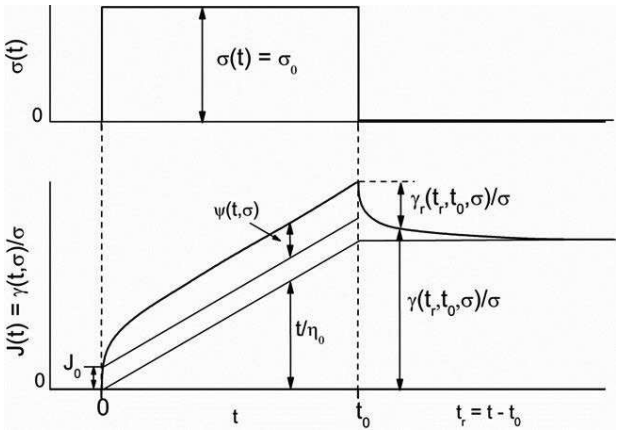

Figure 3.1 Schematic representation of a creep and creep recovery experiment

The deformation itself depends on material properties and on external parameters. Therefore, in the case of creep experiments, the compliance defined as the deformation related to the stress is discussed as the corresponding material-specific function. In Figure 3.1 the creep compliance

$$J(t,\sigma) = \gamma(t,\sigma)/\sigma \tag{3.1}$$

is plotted, with the variable σ being the constant shear stress applied and γ the resulting total shear. According to the Boltzmann superposition principle the creep compliance can be written as (see, e. g., [3.1])

$$J(t,\sigma) = \frac{\gamma(t,\sigma)}{\sigma} = J_0 + \psi(t,\sigma) + \frac{t}{\eta(\sigma)} \tag{3.2}$$

J_0 is the instantaneous compliance, $\psi(t,\sigma)$ the time-dependent recoverable compliance or creep function, and $\eta(\sigma)$ the viscosity. This additivity is visualized in Figure 3.1. It should be mentioned, however, that the superposition principle was derived by Boltzmann for the linear case, in which the creep function and the viscosity are independent of the stress applied. Many experimental results have shown that the decomposition of the creep compliance as given by Equation 3.2 can be used in the nonlinear regime too.

Because the instantaneous compliance is comparatively small and the creep function attains a constant value after some time, for long enough creep times the viscous part dominates the compliance and the viscosity can be obtained from Equation 3.2:

$$\eta(\sigma) = \lim_{t\to\infty} \frac{t}{J(t,\sigma)} \tag{3.3}$$

For correspondingly small stresses in the linear regime, the zero-shear viscosity η_0 follows as

$$\eta_0 = \lim_{\substack{t\to\infty \\ \sigma\to 0}} \frac{t}{J(t,\sigma)} \tag{3.4}$$

In the linear regime the creep function can be described numerically by

$$\psi(t) = \sum_{i=1}^{m} J_i \left(1 - e^{-t/\tau_i}\right) \tag{3.5}$$

with τ_i being discrete retardation times and J_i the corresponding retardation strengths. For a continuous retardation spectrum it follows:

$$\psi(t)=\int_0^\infty f(\tau)\left[1-e^{t/\tau}\right]d\tau \tag{3.6}$$

with the retardation function $f(\tau)$.

The recoverable portion of shear γ_r and therewith the recoverable compliance J_r as functions of the recovery time t_r are dependent in general on the stress σ and the time t_0 of the preceding creep; that means

$$J_r(t_r,t_0,\sigma)=\frac{\gamma_r(t_r,t_0,\sigma)}{\sigma} \tag{3.7}$$

Because the recoverable compliance is defined as the difference between the total compliance and the viscous portion, Equation 3.7 can be written as

$$J_r(t_r,t_0,\sigma)=\frac{\gamma_r(t_r,t_0,\sigma)}{\sigma}=J_0+\psi(t_r,t_0,\sigma) \tag{3.8}$$

For polymer melts and solutions the time-dependent recoverable compliance attains a constant value at sufficiently long creep and recovery times, and one gets for the steady-state recoverable compliance:

$$J_e(\sigma)=\lim_{\substack{t_r\to\infty\\ t_0\to\infty}} J_r(t_r,t_0,\sigma) \tag{3.9}$$

and for the linear steady-state recoverable compliance:

$$J_e^0=\lim_{\sigma\to 0} J_e(\sigma) \tag{3.10}$$

This quantity is of great interest insofar as it is related to the retardation spectrum $f(\tau)$ by

$$J_e^0=J_0+\int_0^\infty f(\tau)d\tau \tag{3.11}$$

where τ designates the retardation time. For a discrete retardation spectrum one can write, according to Equation 3.5,

$$J_e^0=J_0+\sum_{i=1}^{m} J_i \tag{3.12}$$

with J_i being the retardation strengths. More detailed information on the derivation of these relations can be found in [3.1], for example. For polymer melts the

instantaneous compliance J_0 is negligibly small in comparison with the time-dependent recoverable compliance. Thus, from creep recovery experiments in the linear range the retardation spectrum can be determined directly, which is a fingerprint of molecular motions. That is the reason why measurements of the recoverable compliance have found much attention recently as a rheological tool for the characterization of polymers. Examples are given in Section 10.3.3.

In the linear steady-state regime the creep compliance can be written as

$$J(t) = J_e^0 + t/\eta_0 = J_e^0(1 + t/\tau_e) \tag{3.13}$$

where

$$\tau_e = \eta_0 J_e^0 \tag{3.14}$$

is defined as the longest retardation time according to the Voigt-Kelvin model (see, e.g., [3.1]), with η_0 being the zero-shear viscosity.

Three distinct times are used to discuss creep recovery: t describes the time scale of the experiment and t_0 is assigned to the duration of the creep experiment. Then, the recovery time follows $t_r = t - t_0$ as it is obvious from Figure 3.1 and Figure 3.2. As a matter of convention, for recovery and creep the same time scales are used, and then creep compliance and recoverable compliance can be compared conveniently.

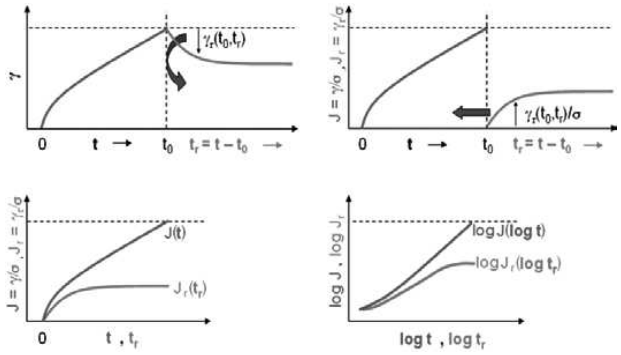

Figure 3.2 Different representations of a creep experiment

As sketched in Figure 3.2, the strain γ increases during creep and consequently the compliance J as the corresponding material-specific function shows a similar behavior. During recovery the total strain decreases, but the recoverable strain γ_r becomes larger. Thus, the recoverable compliance is a material-specific function increasing with time and, therefore, it is reasonable to present J_r on the same scale

Table 6.1 Characteristic Molecular Data of PS I and PS II

	M_w [kg/mol]	M_w / M_n	D_e^0 [Pa^{-1}]
PS I	74	1.2	$6.9 \cdot 10^{-6}$
PS II	39	1.1	$1.1 \cdot 10^{-4}$

Reprinted with permission from [6.27]; copyright 1980 The Society of Rheology.

PS II is distinguished from PS I by a distinct high molar mass component, while PS I shows a weak high molar mass tail sometimes found with anionic polystyrenes. The high molar mass component of PS II is not reflected by the polydispersity index (cf. Table 6.1), but it has a significant effect on the elastic properties as can be seen from the linear steady-state recoverable elongational compliance D_e^0 (cf. Equation 3.51) listed in Table 6.1. For PS II this quantity is higher by a factor of 16 than for PS I. These results are in accordance with those on polystyrene blends presented in Figure 6.12.

The technique of measuring recoverable elongations is described in Section 4.2.6. The compliances in Table 6.1 were measured at a tensile stress of $\sigma_E = 10^3$ Pa, which was found to be in the linear range of deformation for the narrowly distributed polystyrenes [6.27].

6.3.2 Nonlinear Elastic Properties

As was shown in Figure 4.3 for a PP, the recoverable compliance $J_r(t)$ is stress-independent for small stresses and then distinctly decreases with stress. The nonlinear steady-state values are attained at recovery times shorter than in the linear range. From Figure 5.1 it can be concluded for a commercial polypropylene that the stress dependence of J_e is more distinct than that of the shear viscosity η. It is well-established that the viscosity decrease with shear rate or stress, respectively, becomes more pronounced the broader the molar mass distribution. This is demonstrated in the left part of Figure 6.15 for the three polypropylenes PP 2, PP 4, and PP 6 with the polydispersity indices 3.5, 6.4, and 7.7, respectively [6.7]. For a clearer presentation, the viscosities were normalized by their zero-shear values η_0. At the shear stress of 10^3 Pa, η has decreased by about 30% for the sample with the narrowest distribution and by 60% for that with the broadest one.

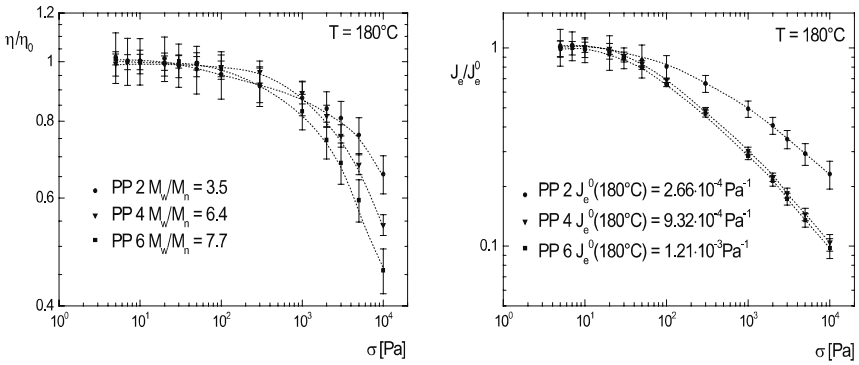

Figure 6.15 Normalized viscosity η (left) and normalized steady-state recoverable compliance J_e (right) as functions of shear stress σ for three polypropylenes with the different polydispersity indices given in the inset [6.7]

The stress dependence of the compliance is much more pronounced than that of the viscosity, as becomes obvious from the right part of Figure 6.15. Here the steady-state recoverable compliance normalized by its linear value is plotted as a function of stress. For the smallest molar mass distribution it becomes smaller by about 80% and even 90% for the broader one at $\sigma = 10^3$ Pa. In the inset of Figure 6.15, the J_e^0 of the three samples is listed. J_e^0 increases by a factor of 3.5 from PP 2 to PP 4, but only by a factor of 1.3 from PP 4 to PP 6. These differences in the linear quantities are reflected by the compliances in the nonlinear regime, too, presented in Figure 6.15.

Considering the transition from the linear to the nonlinear regime it is obvious for the viscosities that the critical stress becomes lower with increasing polydispersity. The same can be observed for the recoverable compliances, but in general a deviation from the linear range is observed at stresses lower than for the viscosity.

A behavior similar to that of the polypropylenes is presented for the metallocene-polymerized linear low density polyethylenes in Figure 6.16. Their molecular data are given in Table 6.2. According to the polymerization technique, long-chain branching is not to be expected and could not be found analytically. As seen from the data in Table 6.2, J_e^0 increases with the polydispersity index, which reflects the molar mass distributions of the equally polymerized polyethylenes. Like for the polypropylenes in Figure 6.15, the sample with the broadest distribution exhibits the strongest stress dependence of the recoverable compliance and starts to deviate from the linear behavior at the smallest stress. The mLLDPE with a polydispersity index between the two others behaves as expected. These results may allow the conclusion that for the three polyethylenes the polydispersity indices mirror the distributions.

Table 6.2 Characteristic Data of Metallocene Polymerized Linear Low Density Polyethylenes with Hexene as Comonomer [6.7]

	M_w [kg/mol]	M_w / M_n	J_e^0 [10^{-5} Pa^{-1}]
mLLDPE 1	69	2.2	2.0
mLLDPE 4	116	2.5	3.0
mLLDPE 5	124	2.9	4.5

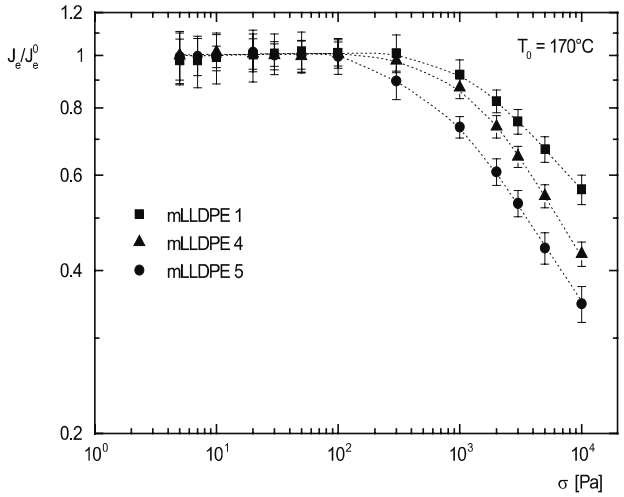

Figure 6.16 Normalized recoverable compliance as a function of shear stress for the three metallocene linear low density polyethylenes (mLLDPE) whose molecular data are given in Table 6.2 [6.7]

Another function describing nonlinearity is the damping function $h(\gamma)$ defined by Equation 5.1. In [6.17] it is shown for a series of linear polyethylenes and polypropylenes that $h(\gamma)$ does not depend on the molar mass distribution. The same can be concluded from investigations on polystyrenes in [6.26].

A typical nonlinear elastic quantity is extrudate swell. As already mentioned in Section 6.2.2, in which the influence of molar mass on nonlinear elastic properties is discussed, there are not many studies in the literature on the extrudate swell of well-defined samples and some of them are even contradictory to each other. For example, in [6.18] it is reported for HDPE that the extrudate swell decreases with increasing M_w/M_n. Just the opposite behavior is found for HDPE in [6.19]. An insight into the complexity of the relations may be obtained from [6.28], where it was shown on binary blends of HDPE prepared by Ziegler-Natta catalysts that for a fixed composition the extrudate swell reaches a maximum as a function of the molar mass of the higher molar mass component. Additionally, it came out that for

two given blend components the higher molar mass fraction, which was changed between 0.3 and 0.6, has some influence on the extrudate swell. The extrudate swell was determined at a shear rate of 300 s^{-1} compared to 3 s^{-1} in [6.18] and 3 s^{-1} and 153 s^{-1} in [6.19]. Furthermore, the geometries of the capillaries used were different. According to Section 5.6, these different experimental conditions make a quantitative comparison of the results not meaningful. Nevertheless, the results on the blends may throw some light on the contrary findings from the literature on the HDPE described above. Due to the various structural features of commercial HDPE, comprising rather often broad molar mass distributions and small amounts of branching, their molecular compositions may be different, giving rise to an extrudate swell increasing or decreasing with M_w/M_n. Such an explanation is not satisfactory, however, neither from a practical nor from a fundamental point of view. Therefore, measurements on polystyrene being linear by nature may be able to explore some aspects of the effects of the molar mass distribution on extrudate swell.

The extrudate swell of two polystyrenes with very similar molar masses M_w, but different molar mass distributions, is presented in Figure 6.17 [6.2]. It is evident that the broader molar mass distribution results in a significantly higher extrudate swell. Similar to the results in Figure 6.6, the measured data can be described by a straight line in the double-logarithmic plot chosen, representing a power law between extrudate swell and shear stress at the wall of the capillary. For the reasons mentioned before, this relationship is empirical and valid only in a limited range of stresses. The viscosity functions of the two different polystyrenes presented in Figure 6.17 are discussed in [6.29].

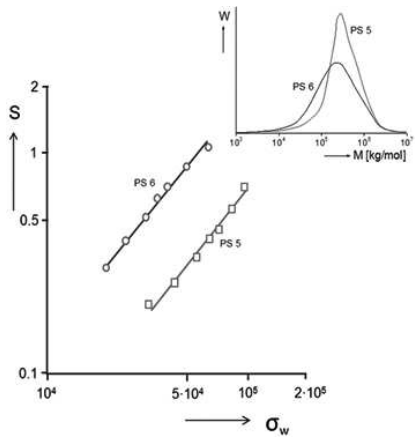

Figure 6.17 Extrudate swell $S = d/d_0 - 1$ as a function of the stress σ_w at the wall of a capillary with the length to radius ratio $L/R = 20$ for two polystyrenes of similar molar masses M_w, but different molar mass distributions. The extrusion temperature was 190 °C. Reprinted from [6.2] with permission from Springer Nature

8 Elastic Behavior and Its Relevance for Various Applications

8.1 Creep Recovery Experiments as a Contribution to Molecular Analysis

Measurements of creep recovery have the advantage that the time dependence of the viscoelastic behavior of polymer melts can be obtained with high accuracy, because the viscous deformation does not mask the elastic effects, which may be comparatively small. Furthermore, the creep and creep recovery, respectively, can be extended to long experimental times, which are only limited by the thermal stability of a sample. Thus, processes with long retardation times can be investigated. The features of creep recovery and its analytical power are demonstrated in the following on a linear low density polyethylene (LLDPE) in comparison with a typical low density long-chain branched polyethylene (LDPE).

8.1.1 Creep Recovery Compliance

The LDPE considered is a common high pressure polyethylene polymerized in a tubular reactor. The LLDPE studied is an ethylene/octene copolymer synthesized by a Ziegler-Natta catalyst. The LDPE has a polydispersity index of $M_w / M_n = 14$ and for the LLDPE $M_w / M_n = 3$ is found [8.1]. The long-chain branches of the LDPE are arranged in a tree-like structure, while for the LLDPE it can be assumed that even a small amount of long-chain branches is excluded due to the polymerization technique used. The GPC traces do not show any indication of a distinct high molar mass component in the two materials [8.1].

As discussed before (see Section 4.2.1), the creep recovery curve depends on the previous creep time t_0 if the steady state has not been reached. This feature is demonstrated in Figure 8.1 for the LLDPE studied in the linear range of deformation. In comparison with Figure 4.2 the recovery curves look different. At creep times t_0 around 100 s a steady-state compliance, independent from the previous creep, seems to be approached (see the filled circles and triangles in Figure 8.1).

But then the steady-state compliance distinctly increases with t_0 again. This behavior becomes more evident from Figure 8.2. In this figure, the steady-state recoverable compliance J_e is plotted linearly as a function of the creep time t_0 presented on a logarithmic scale.

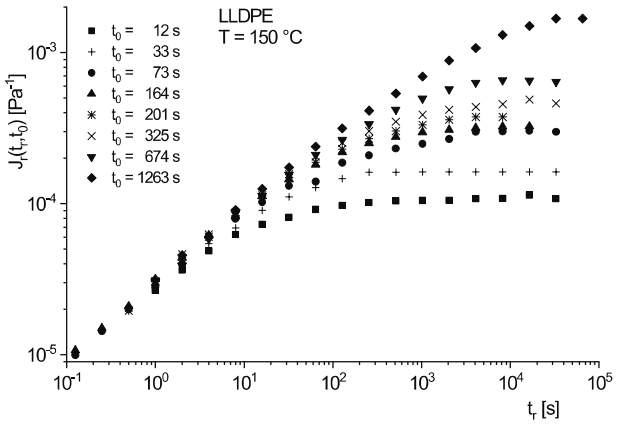

Figure 8.1 Creep recovery compliance J_r in the linear range of deformation as a function of the recovery time t_r for the LLDPE at different creep times t_0. Reprinted from [8.1] with permission from Springer Nature

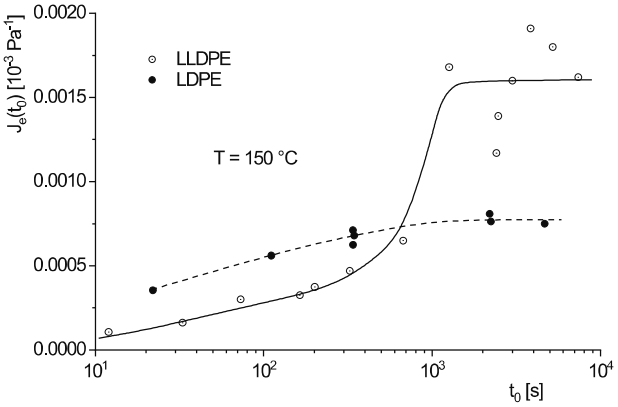

Figure 8.2 Steady-state recoverable compliance J_e as a function of the creep time t_0 in the linear range of deformation for the LLDPE and the LDPE. Reprinted from [8.1] with permission from Springer Nature

For the LDPE a continuous increase in J_e up to a plateau is found. The compliance of the LLDPE increases moderately first, but then jumps up steeply and within the scatter of the experiments reaches a plateau for long creep times, which is distinctly higher than that of the LDPE. These results lead to the conclusion that for the LLDPE two deformation processes may be assumed, the time dependencies of which are different.

It is interesting to see how the different ecovery behavior of each of the two samples as a function of the previous creep time in Figure 8.2 is reflected by the dependence of the recoverable compliance J_r on the recovery time t_r, represented in Figure 8.3. At shorter times, the J_r of the LDPE is higher than that of the LLDPE. But the steady-state value and the time at which it is reached are significantly smaller than for the LLDPE. In the double-logarithmic plot of Figure 8.3 the step of the compliance for the LLDPE revealed by the linear presentation in Figure 8.2 is hard to detect. It is indicated by a slight change in slope, marked by the arrow.

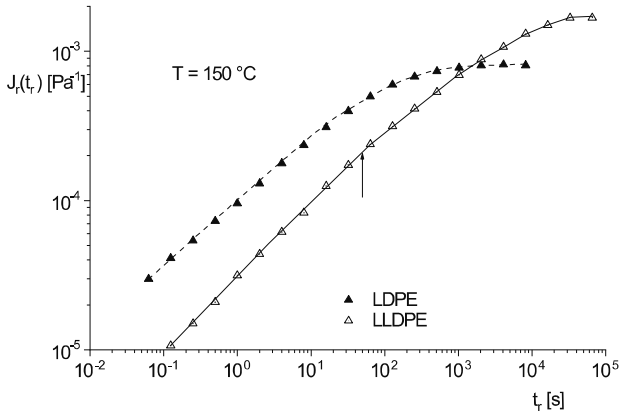

Figure 8.3 Recoverable compliance J_r as a function of the recovery time t_r in the linear range of deformation for LDPE and LLDPE in a double-logarithmic plot. Reprinted from [8.1] with permission from Springer Nature

8.1.2 Retardation Spectra

Some evidence for the two retardation processes that are evident from Figure 8.2 is obtained from the retardation spectra in Figure 8.4. They were calculated according to [8.2] and [8.3], based on the relation

$$J_r(t_r) = \sum_{k=1}^{n} J_k \left(1 - e^{-t_r/\tau_k}\right) \tag{8.1}$$

with τ_k being the discrete retardation times and J_k the retardation strengths. Equation 8.1 follows from Equation 3.5 according to

$$J_r(t_r) = J_0 + \psi(t_r) \tag{8.2}$$

with the instantaneous compliance J_0 being negligibly small for polymer melts.

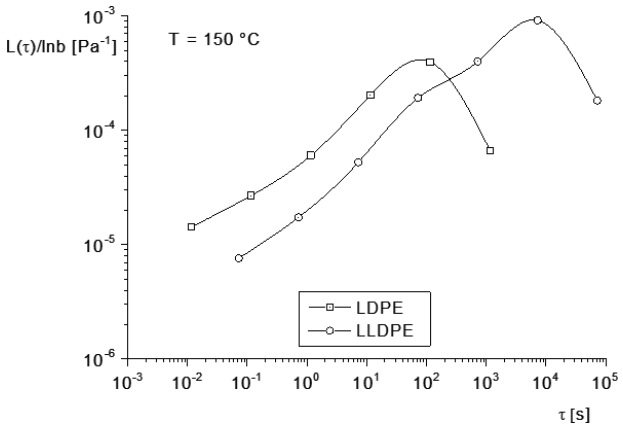

Figure 8.4 Retardation spectra of the LDPE and the LLDPE calculated from Figure 8.3. The symbols represent the discrete retardation strengths for the chosen retardation times, and the full lines describe the continuous retardation spectra $L(\tau)/\ln b$, where the step width b was chosen as 10. Reprinted from [8.1] with permission from Springer Nature

The full lines describe the continuous retardation spectra according to Equation 6.8:

$$J(\tau) = \int_{-\infty}^{\infty} L(\tau) d\ln(\tau)$$

For the LDPE a "smooth" spectrum is obtained, while for the LLDPE a shoulder becomes visible, which indicates two retardation processes superposing each other.

As it is demonstrated by Figure 8.2 and Figure 8.4, measurements of the recoverable compliance are a sensitive tool to detect different retardation processes within a polymer melt. However, it is not possible to draw conclusions from the retardation spectra on the relevant molecular structures underlying the processes. For such kind of analysis other methods have to be applied, as shown and discussed in [8.1]. From differential scanning calorimetry (DSC) and temperature rising elution fractionation (TREF) it was concluded that the LLDPE may consist of two species with different concentrations of comonomers, which are not miscible with each other and give rise to the two different retardation processes observed.

8.1.3 Calculation of Dynamic-Mechanical Quantities from Retardation Spectra

According to the linear theory of viscoelasticity, the real part J' and the imaginary part J'' of the complex compliance $|J^*|$ as functions of the angular frequency ω are related to the discrete retardation spectrum, defined in Equation 8.1, by (see, e. g., [8.4]):

$$J'(\omega) = \sum_{k=1}^{n} J_k \frac{1}{1+\omega^2\tau_k^2} \tag{8.3}$$

and

$$J''(\omega) = \frac{1}{\omega\eta_0} + \sum_{k=1}^{n} J_k \frac{\omega\tau_k}{1+\omega^2\tau_k^2} \tag{8.4}$$

with η_0 being the zero-shear viscosity.

For the LLDPE, J' and J'', calculated according to Equation 8.3 and Equation 8.4 from the spectrum in Figure 8.4, are presented in Figure 8.5 (open symbols) by setting

$$\omega_k = 1/\tau_k \tag{8.5}$$

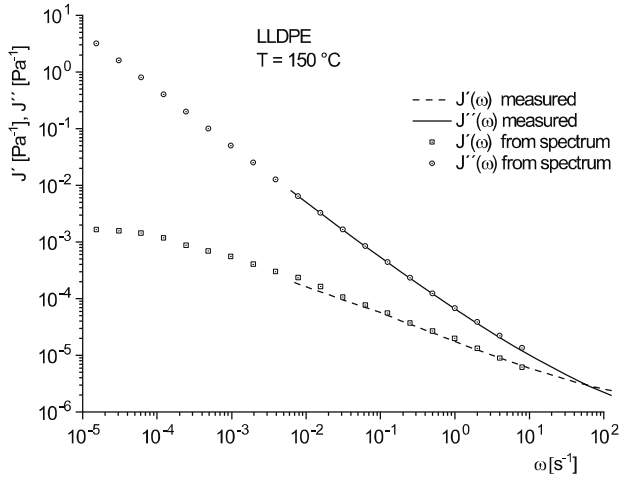

Figure 8.5 Real part J' and imaginary part J'' of the complex compliance calculated from the discrete retardation spectrum in Figure 8.4 as functions of the discrete angular frequencies ω_k (symbols) in comparison with the functions measured with a rotational rheometer (curves)

in the following, the emphasis lies on elastic properties of various combinations of matrices and nanofillers.

10.1 Nanoparticles Investigated

As a reference filler material, silica particles are used. They are produced on an industrial scale by flame pyrolysis and are commercially available. The median diameters d_{50} of the two kinds of beads investigated are 20 and 70 nm [10.3]. The advantage of these particles is their compact spherical structure, which does not change under the stress exerted on them in a melt during flow. They are very suitable for fundamental investigations, but their importance as nanofillers for commercial polymeric materials is rather limited.

Of more practical relevance are nanoclays. Detailed information about the structure of this montmorillonite can be obtained from the corresponding literature ([10.4], for example). Nanoclays consist of many platelets about 1 nm thick, with lateral dimensions of 100 to 500 nm, that are stacked together. To obtain a high specific surface area for interactions with the matrix molecules, the stacks have to be exfoliated as extensively as possible. Procedures for the preparation of polymethylmethacrylate (PMMA) with nanoclay and the control of particle exfoliation and distribution are described in [10.5].

Another widely available natural product with a platelet structure is graphite. The edges of the platelets measure several microns but the thickness is around 200 nm, resulting in aspect ratios between 10 and 20. Graphite consists of layers with thicknesses down to atomic dimensions. The complete exfoliation of the graphite layers is very challenging, but bears a high potential for carbon materials with new properties. In 2004, the first free-standing two-dimensional sheet consisting of one layer of carbon atoms was described, which was obtained from the cleavage of graphite [10.6]. This material is called graphene and is distinguished by large specific surface areas, a high tear strength, remarkable electrical conductivity, and good transparency. Its exploration as a promising new filler for polymeric materials is irrelevant, however, as long as an efficient production on a larger scale is not available. Nevertheless, it follows from [10.7], for example, that interesting properties could be generated in polymeric materials by the addition of graphene-type fillers even if carbon monolayers are not obtained by the cleavage of particularly pretreated graphite.

Another carbon-based filler available in several modifications on an industrial scale is carbon black (CB). An overview of the properties of carbon black is given in [10.8], for example. Carbon black has been used widely in the rubber industry

and, therefore, rheological properties of mainly elastomers filled with CB can be found in the literature ([10.9], for example). A systematic investigation of the rheological properties of a thermoplastic material with carbon black is published in [10.10], using polystyrene as the matrix. However, elastic properties of melts of polymeric materials with carbon black have been investigated only very sparsely. Interpretations of rheological measurements are complex insofar as the primary particles of carbon black with diameters of about 50 nm may form larger agglomerates, an example of which is given in Figure 10.1. The shape of the agglomerates depends on many factors, such as the type of carbon black, the matrix polymer, and the compounding process.

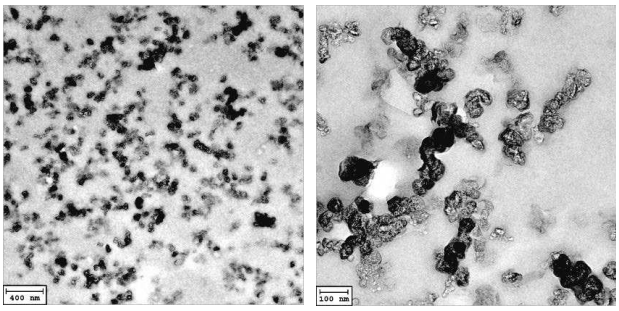

Figure 10.1 Transmission electron micrographs of different magnifications for a PMMA filled with the carbon black PRINTEX XE 2 [10.11] at a volume fraction of $\Phi = 0.05$. Adapted from [10.12]

Aspect ratios of the carbon black agglomerates are difficult to assess, but may be assumed to lie at around 10 to 20. The carbon black aggregates are able to form a three-dimensional network that is decisive for the electrical conductivity of a composite (see [10.5], for example).

Carbon nanotubes (CNT) are nanofillers with potential for interesting applications. They were discovered at the beginning of the 1990s [10.13] and their fundamental properties were investigated in the following years on small amounts manufactured on a laboratory scale. From 2010 onward, CNT have been produced industrially, and since that time it is possible to exploit their potential as fillers in polymeric materials. Due to their graphitic structures, carbon nanotubes can be considered as wrapped up graphene sheets. One distinguishes nanotubes consisting of a single wall (SWCNT) and those with multiple walls (MWCNT) of numbers typically between 3 and 15. The inner diameters of CNT lie at several nm; the outer ones, between 10 and 20 nm. The lengths of the nanotubes are not uniform. They may differ between 1 and more than 10 µm and are prone to breakage during processing in a melt. CNT are materials with nanoscale dimensions in only one direc-

tion. The filament structure of a CNT is the reason for a flexibility that may lead to statistically distributed entanglements of fibers. These morphological features make it difficult to find relations between properties of polymeric materials filled with nanotubes and their geometries.

The short discussion above on the morphology of particle-filled polymer melts addresses the problem of getting a reliable picture of the real filler distribution within a sample. Even in the case of the simple geometry of silica beads the arrangement of the fillers within a sample may be difficult to assess, as has to be concluded from Figure 10.2, which shows the distribution of 2.1 vol % of the silica beads with 20 nm of mean diameter in a PMMA matrix. The silica beads are not totally separated from each other, but form agglomerates of various shapes. The specific surface area of such agglomerate is difficult to assess because of its rugged shape and some kind of porosity, which may offer areas within the pores for interactions with the matrix molecules. In any case, it has to be stated that the diameter of a particle may only represent a nominal quantity and that the real morphology may be dependent on properties of the filler and the matrix and the way of processing. This example throws light on the difficulties which arise in compounding when a good separation of filler particles has to be achieved. The optimal dispersion of nanoparticles is a big problem in polymer processing, particularly when cost-effective processes based on melt extrusion are applied.

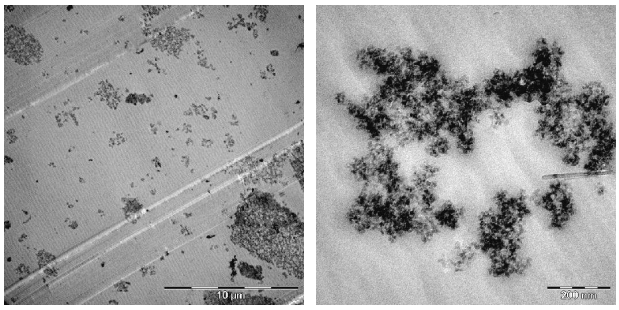

Figure 10.2 Transmission electron micrograph of two magnifications for PMMA filled with silica beads of a nominal diameter of 20 nm. Adapted from [10.3]